Dual-color superresolution microscopy reveals nanoscale organization of mechanosensory podosomes

K. van den Dries[a], S. L. Schwartz[b], J. Byars[c], M.B.M. Meddens[a], M. Bolomini-Vittori[a], D. S. Lidke[b], C. G. Figdor[a], K. A. Lidke[c], and A. Cambi[a,d]

[a]Department of Tumor Immunology, Nijmegen Centre for Molecular Life Sciences, Radboud University Nijmegen Medical Centre, 6500 HB Nijmegen, Netherlands; [b]Department of Pathology and [c]Department of Physics and Astronomy, University of New Mexico, Albuquerque, NM 87131; [d]Nanobiophysics, MIRA Institute for Biomedical Technology and Technical Medicine and MESA+ Institute for Nanotechnology, Faculty of Science and Technology, University of Twente, 7500AE Enschede, Netherlands

ABSTRACT Podosomes are multimolecular mechanosensory assemblies that coordinate mesenchymal migration of tissue-resident dendritic cells. They have a protrusive actin core and an adhesive ring of integrins and adaptor proteins, such as talin and vinculin. We recently demonstrated that core actin oscillations correlate with intensity fluctuations of vinculin but not talin, suggesting different molecular rearrangements for these components. Detailed information on the mutual localization of core and ring components at the nanoscale is lacking. By dual-color direct stochastic optical reconstruction microscopy, we for the first time determined the nanoscale organization of individual podosomes and their spatial arrangement within large clusters formed at the cell–substrate interface. Superresolution imaging of three ring components with respect to actin revealed that the cores are interconnected and linked to the ventral membrane by radiating actin filaments. In core-free areas, $\alpha M\beta 2$ integrin and talin islets are homogeneously distributed, whereas vinculin preferentially localizes proximal to the core and along the radiating actin filaments. Podosome clusters appear as self-organized contact areas, where mechanical cues might be efficiently transduced and redistributed. Our findings call for a reevaluation of the current "core–ring" model and provide a novel structural framework for further understanding the collective behavior of podosome clusters.

INTRODUCTION

Cell–cell and cell–extracellular matrix (ECM) interactions are tightly coordinated by supramolecular assemblies that form at the cellular plasma membrane. Well-known cell–ECM interfaces include focal adhesions, which are integrin-based contacts linked to stress fibers

(Geiger *et al.*, 2009). Cells specialized in crossing cellular boundaries and basement membranes also form other types of adhesion structures known as podosomes—dynamic, dot-shaped adhesion complexes that mediate sensing of extracellular topographical cues and are involved in adhesion to and protrusion in the ECM (Linder *et al.*, 2011; Murphy and Courtneidge, 2011; van den Dries *et al.*, 2012). Unraveling the nanoscale organization of podosome assemblies will provide essential mechanistic insight into their structure–function relationship.

Podosomes have been observed at the contact area between the ECM and various cells of myeloid origin, including dendritic cells (DCs; Trotter, 1981; Marchisio *et al.*, 1984; Gaidano *et al.*, 1990; van Helden *et al.*, 2006). They arrange into higher-ordered structures, such as large clusters in macrophages and DCs or circular belts in osteoclasts (Lakkakorpi *et al.*, 1989; Evans *et al.*, 2003; Burns *et al.*, 2004), suggesting the existence of concerted communication

among podosomes at the mesoscale for which no clear mechanism has been proposed. Individual podosomes comprise two functional modules: a central actin core associated with protrusion, surrounded by a ring of integrins and cytoskeletal adaptor proteins, such as talin and vinculin, associated with adhesion. The core and the ring are believed to be connected by a filamentous actin network (F-actin), where also myosin IIA is found (Gawden-Bone *et al.*, 2010; van den Dries *et al.*, 2013). This actomyosin network has been shown to critically control podosome stiffness oscillations (Labernadie *et al.*, 2010). More recently, our group demonstrated that the interplay between myosin contractility and actin network integrity is also responsible for the concerted intensity oscillations of the actin core and the mechanosensitive zyxin and vinculin in the ring, leaving talin and paxillin levels unaffected. Furthermore, we showed that the intact actin network provided an essential molecular infrastructure for maintaining podosome integrity (van den Dries *et al.*, 2013). Although these data suggest important differences in the molecular arrangements that could further our understanding of podosome function, detailed information on the mutual localization of core and ring components at the nanoscale is lacking.

Podosomal architecture has mainly been investigated by conventional microscopy techniques. Confocal microscopy revealed the distinctive core–ring organization (Marchisio *et al.*, 1984; Pfaff and Jurdic, 2001), and transmission electron microscopy (TEM) showed that podosome cores are characterized by an electron-dense area (Gawden-Bone *et al.*, 2010; Labernadie *et al.*, 2010). Confocal microscopy further revealed a diffuse actin staining, a so-called cloud, that surrounds the cores in osteoclasts (Destaing *et al.*, 2003), and scanning electron microscopy (SEM) later suggested that this cloud comprises a network of actin filaments (Luxenburg *et al.*, 2007; Schmidt *et al.*, 2011). Although TEM and SEM provide nanoscale spatial resolution, the extensive sample treatment is prone to artifacts, and simultaneous labeling of multiple protein species remains challenging. More recently, Bayesian localization microscopy revealed that the podosome rings are highly dynamic on a second time scale (Cox *et al.*, 2012), but the nanoscale organization of the ring components with respect to the actin core and the network of actin filaments has not been investigated.

Direct stochastic optical reconstruction microscopy (dSTORM) belongs to the family of superresolution techniques that exploits the sequential readout of emitters in a sample to achieve a lateral localization accuracy of typically 20 nm (Betzig *et al.*, 2006; Hess *et al.*, 2006; Rust *et al.*, 2006; Heilemann *et al.*, 2008). Here we exploit dSTORM to determine the nanoscale organization of individual podosomes and their spatial arrangement within large clusters formed by primary human monocyte-derived DCs. We determine the localization of actin, αMβ2, which is the predominant integrin at podosomes in DCs (Burns *et al.*, 2004), and the adaptor proteins talin and vinculin. Together the novel structural insights presented here call for a reevaluation of the current core–ring model for podosomes and represent a major step toward a better understanding of podosome adhesive and protrusive machinery. Moreover, our results provide a structural framework for understanding podosome cluster function as a mesoscale mechanosensing apparatus essential for environment probing while crossing cellular boundaries and basement membranes.

RESULTS
Differential localization of ring-associated proteins
To determine the two-dimensional localization of podosome ring components with respect to the core, we seeded DCs onto glass coverslips and subsequently fixed and stained them to simultaneously visualize actin with αMβ2 integrin, talin, or vinculin by confocal microscopy (Figure 1, A–C). Although all the investigated proteins are enriched in podosome clusters compared with nonpodosome areas (Figure 1, A–C, green and orange insets) and are completely excluded from the cores, their staining patterns at the podosome rings differ, with αMβ2 and talin appearing more diffuse than vinculin. To quantify this observation, we analyzed confocal microscopy images by a custom-written quantitative image analysis algorithm (Meddens *et al.*, 2013) and measured the mean fluorescence profile of each component in areas at increasing distance from the core (Figure 1D). As expected, αMβ2, talin, and vinculin are all present in the ring (Figure 1, A–C). Whereas the intensity profiles of αMβ2 and talin display no significant changes at increasing distances from the core, occupying the entire core-free area of the podosome cluster as a carpet, vinculin intensity peaks very close to the core and quickly decays at increasing distances from the core (Figure 1E). Note that the general appearance of podosomes is independent of the surface used to attach the DCs. In fact, podosome formation and composition in cells seeded on uncoated glass coverslips do not differ from podosomes of cells adhered onto polymeric substrates with near–in vivo stiffness (Supplemental Figure S1) or coated with different integrin ligands (Supplemental Figure S2).

Together these results indicate that whereas αMβ2 and talin are homogeneously distributed throughout the podosome cluster, the distribution of vinculin at the core-free area within the podosome cluster is restricted to the most proximal region around the actin core. Together these observations suggest the existence of substructures within the podosome cluster that appear to be differentially populated by various components.

F-actin network as major determinant for differential localization of vinculin and talin
We recently showed that the localization of ring components such as vinculin and talin is differentially affected by the integrity of the F-actin network that interconnects the podosome cores (van den Dries *et al.*, 2013). To investigate the simultaneous localization of vinculin and talin within the same podosome cluster, we visualized both proteins, as well as actin, in DCs before and after addition of low concentration of cytochalasin D (cytoD), which is reported to specifically disrupt the F-actin network (Labernadie *et al.*, 2010; van den Dries *et al.*, 2013). To prevent antibody cross-reactivity, we transfected DCs with vinculin–green fluorescent protein (GFP) and subsequently fixed and stained them with an anti-talin antibody followed by a fluorescent secondary antibody, and with Alexa Fluor 546–conjugated phalloidin to visualize actin. Subsequent confocal microscopy analysis revealed that both proteins are excluded from the podosome cores and confirmed that vinculin and talin differentially localize with respect to the actin cores throughout the entire cluster (Figure 2A). Of importance, after the disruption of the F-actin network, only the localization of talin remains unaffected within the podosome cluster (Figure 2A).

To investigate whether the specific localization of vinculin depends on its actin binding capacity, we coexpressed GFP-tagged wild-type vinculin (VinWT) and the mCherry-tagged tail-less mutant (VinTL) in DCs and examined their localization with respect to actin before and after mild cytoD treatment. As shown in Figure 2B, we observed that VinTL, which has a talin-binding site but lacks the actin-binding site (Bakolitsa *et al.*, 2004), exhibits diffuse localization throughout the entire podosome cluster that is clearly different from that of VinWT but very reminiscent to the talin (and integrin) organization. Furthermore, unlike VinWT, VinTL localization was largely unaffected by the disruption of the actin network (Figure 2B),
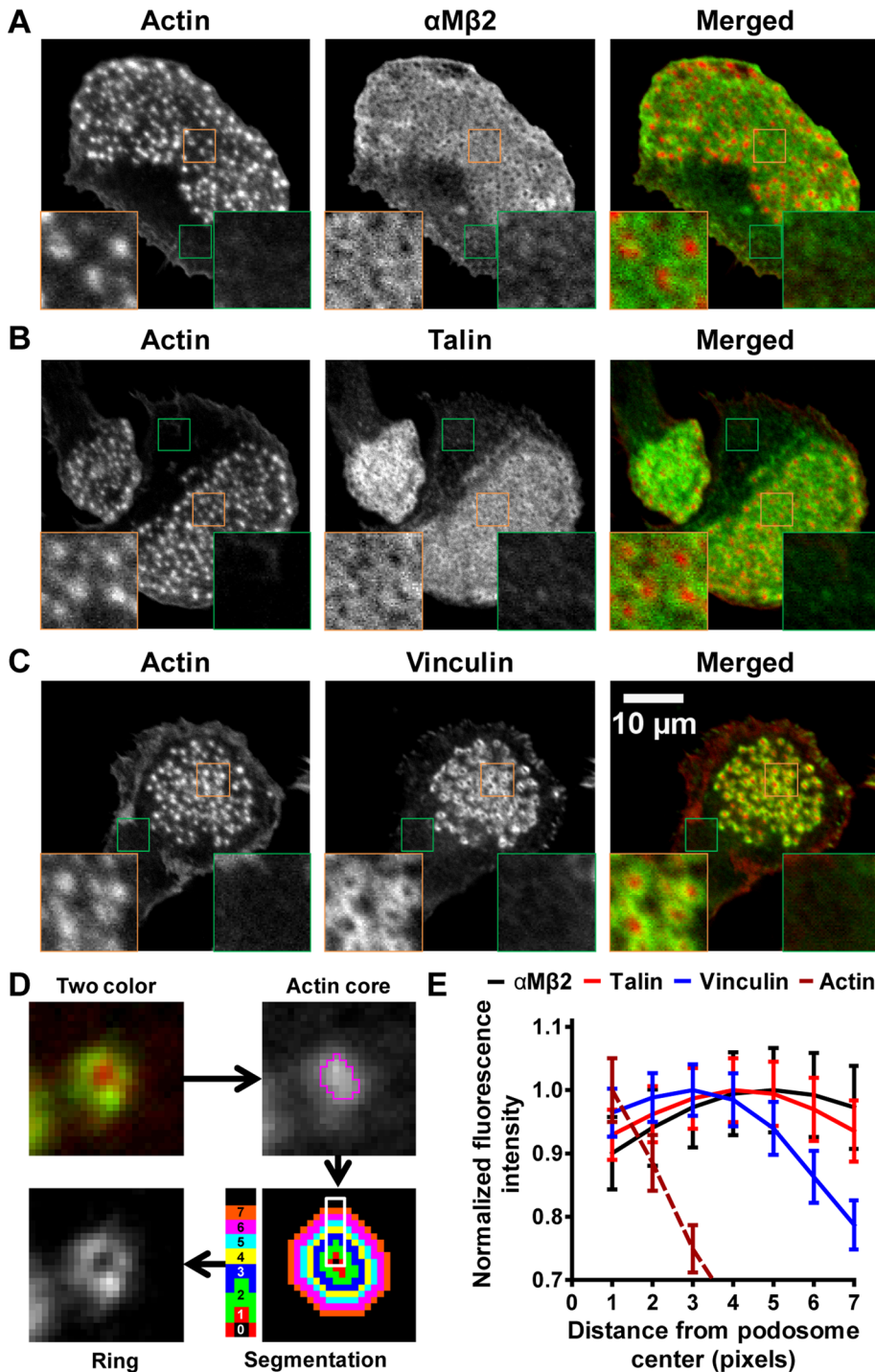
FIGURE 1: Differential distribution of αMβ2, talin, and vinculin within the podosome cluster. Immature DCs were seeded onto glass coverslips, fixed, and stained with Texas red–conjugated phalloidin and specific monoclonal antibodies to visualize actin with (A) αMβ2, (B) talin, and (C) vinculin. Insets depict enlargements of a podosome (orange) and a nonpodosome area (green). (D) A custom-written quantitative image analysis algorithm was used to segment the podosome cores in confocal microscopy images. The segmented cores were subsequently dilated with 1-pixel steps using a distance transform. These segmentations were used to calculate the average fluorescence intensity of the ring components at increasing distances from the core. (E) Average fluorescence intensity levels of αMβ2, talin, and vinculin at increasing distances from the podosome core center calculated for at least 1000 individual podosomes in multiple cells as described in D. The data were normalized to the maximum fluorescence intensity, and error bars indicate SEM.

demonstrating that the actin-binding capacity of vinculin is essential for its specific well-defined localization close to the podosome core. Together these results demonstrate that the actin network is the major determinant for the differential localization of vinculin and talin within the podosome cluster and that talin and vinculin localization is regulated by different mechanisms. These data also suggest the existence of substructures of ring components differentially populating the podosome cluster.

Podosome clusters comprise dense actin cores with radiating actin filaments

To gain better insight into the nanoscale organization and mutual localization of αMβ2, talin, and vinculin, we performed dSTORM at sites of podosome clusters. First, we analyzed the localization of F-actin, the most prominent component of the podosome cluster and widely used to identify podosomes in cells. Owing to the very high emitter density within the samples, we successfully used a multifitting algorithm (Huang *et al.*, 2011) to resolve the actin structures within the podosome cluster (Supplemental Figure S3).

As expected, actin is highly enriched at the podosome cores (Figure 3A). By calculating the perimeter and diameter of the cores, we found them to be very heterogeneous (Figure 3E and Supplemental Figure S4A). The core perimeter values spread between a minimum of ~600 nm and a maximum of 4 μm (Figure 3E), whereas the minimum and maximum diameter values measured were ~200 and 800 nm, respectively. Of importance, cross-correlating the perimeter with diameter values revealed that the two parameters are directly correlated (Supplemental Figure S4B). Furthermore, by fitting the size value distributions with a bimodal Gaussian function, we were able to identify two main podosome populations. The smallest population had an average perimeter of 1.75 ± 0.71 μm and an average diameter of 303 ± 81.5 nm, whereas the largest podosome population had an average perimeter of 2.11 ± 0.19 μm and an average diameter of 549 ± 94.6 nm (Figure 3E and Supplemental Figure S4A). Of interest, we also identified two different podosome populations based on circularity (Figure 3F) and found a negative correlation between perimeter and circularity (Figure 3G), indicating that the small podosomes are circular (Figure 3G, inset 1), whereas the large podosomes are more elongated (Figure 3G, inset 2). The
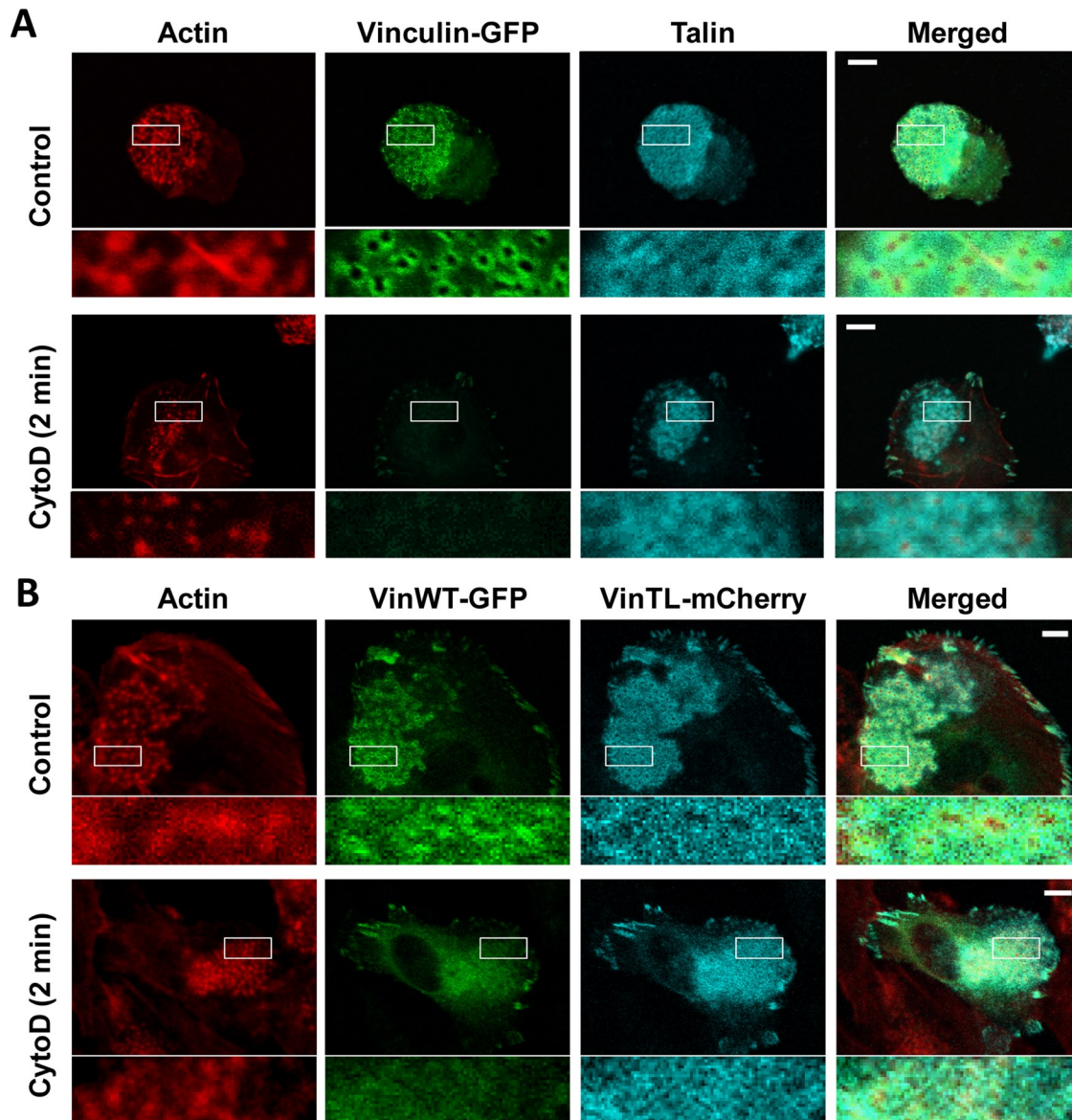
FIGURE 2: F-actin network major determinant for differential localization of vinculin and talin. (A) Immature DCs were transfected with vinculin-GFP and left untreated or stimulated with cytoD for 2 min. Cells were subsequently stained with a talin antibody and Alexa Fluor 546–conjugated phalloidin to visualize talin and actin, respectively. Representative images for both conditions are depicted. (B) Immature DCs were transfected with VinWT-GFP and VinTL-mCherry and left untreated or stimulated with cytoD for 2 min. Cells were subsequently stained with Alexa Fluor 633–conjugated phalloidin to visualize actin. Representative images for both conditions are depicted.

observed heterogeneity of the core parameters presumably reflects the dynamic nature of podosomes (Evans *et al.*, 2003; Kopp *et al.*, 2006). Continuous formation and dissolution within the cluster are most likely the major determinants of the observed large range in core perimeter and diameter. The large, elongated population of podosomes could be ascribed to podosomes that were undergoing fusion or fission at the moment of sample fixation.

Previous studies in osteoclasts and macrophages indicated the existence of a poorly defined actin cloud in between podosome cores (Destaing *et al.*, 2003; Saltel *et al.*, 2008). The extremely bright signal originating from the dense actin core overruled the weaker signal coming from the actin cloud, preventing a detailed characterization of this region by conventional fluorescence microscopy. By dSTORM, we clearly distinguished an F-actin network in between the podosomes, which consists of filaments that are highly heteroge-

neous in both length and thickness. Typically, 5–10 actin filaments with a thickness ranging between 0.1 and 0.2 μm radiate from single podosome cores (Figure 3, B and C). The length of the filaments ranges between 0.1 and 0.8 μm, with an average of 0.43 ± 0.19 μm. Of importance and in contrast to previous observations in osteoclasts (Luxenburg *et al.*, 2007), we found that virtually all podosome cores were interconnected with one or more neighboring cores via actin filaments (Figure 3D). These interconnecting filaments appeared to be much thicker (0.35 μm), suggesting that they are reinforced to provide stability to the connected podosome cores. Alternatively, these thicker filaments could be formed by multiple filaments so intimately bundled that they cannot be spatially resolved. The high level of interconnection between individual cores supports a hypothesis in which clusters of podosomes act as a mesoscale mechanosensing apparatus in which mechanical forces are continuously
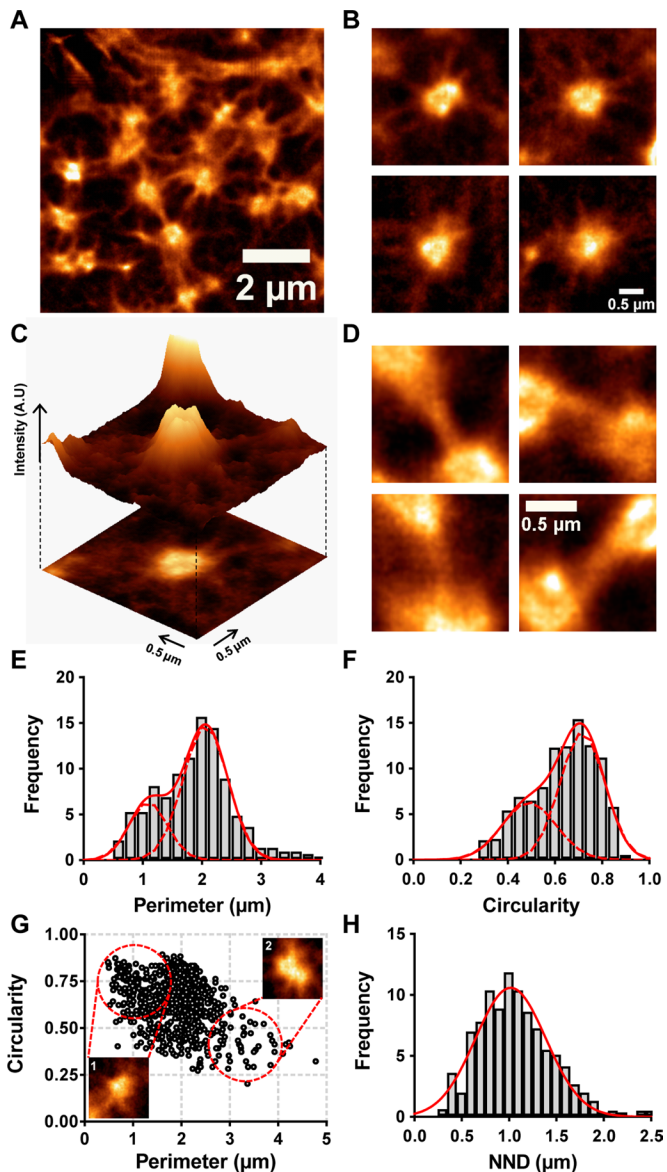
FIGURE 3: The podosome cluster comprises of dense actin cores and an interconnecting F-actin network. (A) Immature DCs were seeded on glass coverslips for 3 h, fixed, and stained for Alexa Fluor 488–conjugated phalloidin to visualize actin. Shown is the dSTORM reconstruction of a part of a representative podosome cluster with podosome cores and associated network. Details on the representation of the dSTORM reconstruction images are given in Supplemental Figure S1. (B) Magnification of individual podosomes within a cluster to show the actin filaments that radiate from the podosome cores. (C) Three-dimensional projection of a dSTORM image that displays a central podosome core and radiating actin filaments. The upper right podosome in Figure 1B is used for this projection. (D) Magnification of actin filaments that interconnect multiple podosomes. (E, F) The podosome core perimeter (E) and circularity (F) were determined for ~700 individual podosomes. The distributions were fitted with a sum of two Gaussians formula using GraphPad Prism software. Shown are the frequency distributions and the fit of the data (solid line). The two individual Gaussians are also shown (dashed line). (G) Correlation of the podosome core circularity and perimeter. (H) The podosome nearest-neighbor distance (NND) was determined using the center of mass of >700 individual podosomes. Shown are the frequency distribution and the Gaussian fit of the data (solid red line).

transmitted and redistributed. Moreover, communication between podosome cores could efficiently facilitate the simultaneous formation of contiguous podosomes that we often observe at the edge of a cluster (Supplemental Figure S5 and Supplemental Video S1).

To better characterize the organization of the podosome cores in relation to the actin filaments we calculated the nearest-neighbor distance for >700 podosomes in multiple cells. We found that the distance between podosomes is distributed around 1.02 ± 0.37 μm (Figure 3H), which is about twice the average length of the radiating actin filaments. Thus, the average interpodosome distance seems to be directly correlated with the length of the actin filaments that radiate from the podosome cores, suggesting that the F-actin network may play an important role in spacing the podosomes within the cluster.

Nanoscale topography of integrin αMβ2 and talin within the podosome cluster

The αMβ2 integrin is the predominant adhesion receptor present in podosomes within DCs, and its specific recruitment to podosomes has been shown to be essential for the binding of DCs to its main counterreceptor, ICAM-1 (Burns et al., 2004). Although αMβ2 is supposed to be localized at the podosome ring (Figure 1A), its spatial organization pattern within podosome clusters is poorly defined. Here we determined the two-dimensional localization of αMβ2 with respect to the actin core by dual-color dSTORM. We performed double staining of actin and αMβ2 in adherent and fixed DCs and collected the image series for the two channels to reconstruct the dSTORM images. We found that αMβ2 organizes in small islets that have a seemingly random distribution within the podosome cluster but are completely excluded from the podosome core area, as indicated by the dark regions within the cluster (Figure 4, A–C). Besides αMβ2, β1 integrins have also been documented at sites of podosomes in DCs (van Helden et al., 2006), and although they are not specifically enriched in the podosome cluster like αMβ2 (Supplemental Figure S7A), their presence suggests that multiple classes of integrins provide the podosome cluster with a large and dense adhesive plaque to strongly connect the cell to the underlying substrate.

Talin directly binds to integrins and is implicated in the initiation of adhesion formation, either by activating integrins or by binding to already activated integrins (Nayal et al., 2004; Moser et al., 2009). In contrast to integrins, talin has the ability to directly bind to F-actin and is therefore essential for linking integrins to the actin cytoskeleton. Of interest, dSTORM analysis showed that talin localization very much resembles αMβ2 localization. Islets of talin were homogeneously distributed within the podosome cluster but completely excluded from the podosome cores (Figure 4, D–F).

Together these results indicate that the podosome adhesive apparatus is not restricted to a small, ring-like area directly surrounding the podosome core but instead spreads through the entire podosome cluster as a carpet. Of importance, αMβ2 and talin are completely excluded from the protrusive podosome core areas, indicating that the adhesive and protrusive apparatus of podosomes are spatially well separated. Moreover, the carpet could also facilitate the anchoring of new actin fibers radiating from an existing podosome and assisting the simultaneous formation of new contiguous podosomes (Supplemental Figure S5 and Supplemental Video S1).

Vinculin localizes to the direct vicinity of podosome actin cores and along the radiating actin filaments

Vinculin is a mechanosensitive molecule that reinforces the link between the integrins and the actin cytoskeleton by binding to talin
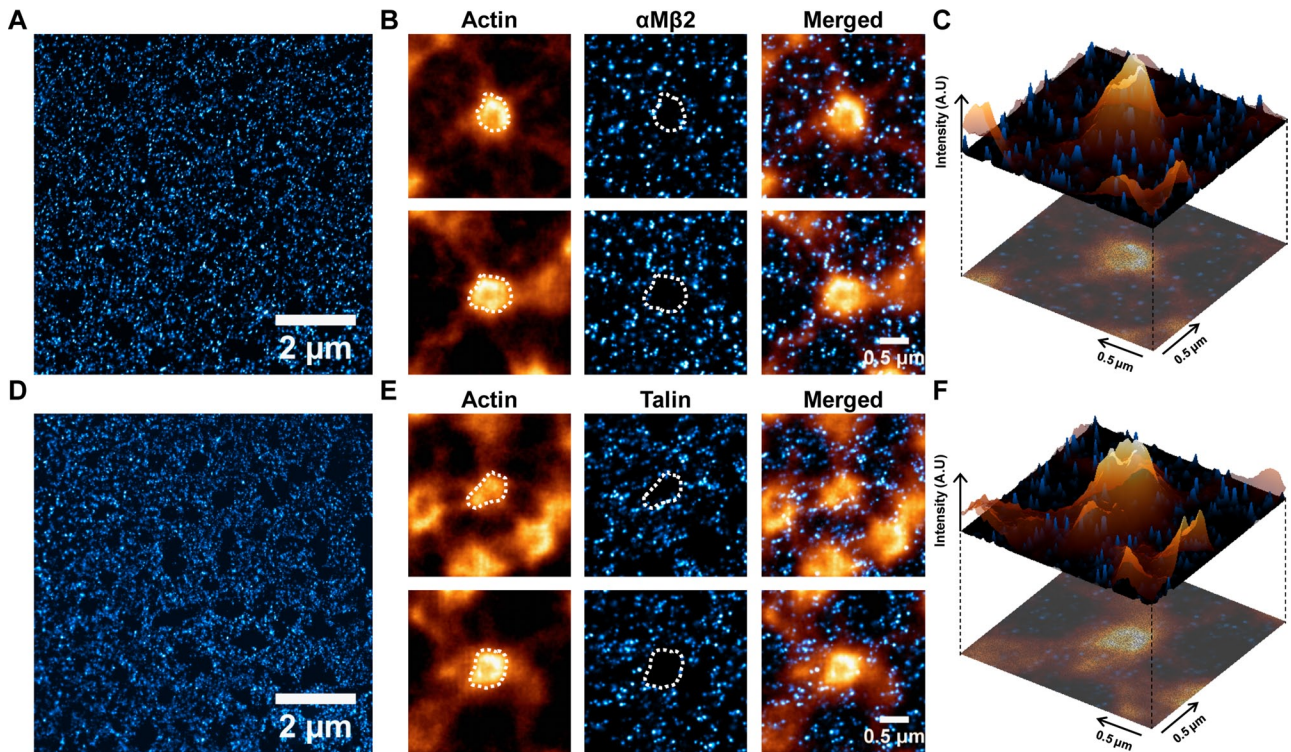
FIGURE 4: αMβ2 and talin are localized in homogeneously distributed islets within the podosome cluster. (A) dSTORM image of αMβ2 within the podosome cluster of DCs. (B) Dual-color dSTORM images of αMβ2 and F-actin. Shown are two representative podosomes within a cluster. (C) Three-dimensional projection of a dual-color dSTORM image that displays a central core of F-actin surrounded by many αMβ2 islets. The upper image in B was used for this projection. (D) dSTORM image of talin within the podosome cluster of DCs. (E) Dual-color dSTORM images of talin and F-actin. Shown are two representative podosomes within a cluster. (F) Three-dimensional projection of a dual-color dSTORM image that displays a central core of F-actin surrounded by many talin islets. The lower image in E was used for this projection.

with its head domain and to actin with its tail domain (Humphries *et al.*, 2007; Kanchanawong *et al.*, 2010). Talin contains many vinculin-binding domains to ensure signal amplification during adhesion formation (Gingras *et al.*, 2005; Patel *et al.*, 2006), and it is generally believed that only stretched talin is capable of binding vinculin (del Rio *et al.*, 2009; Margadant *et al.*, 2011). Inspection of the nanoscale localization of vinculin with respect to podosome actin by dual-color dSTORM revealed that in sharp contrast to αMβ2 and talin, vinculin molecules are not homogeneously distributed within the podosome cluster (Figure 5, A–E).

To better quantify these differences, we calculated the average localization density of the three ring components at increasing distances from the podosome core (Figure 6). We found that the levels of αMβ2 are relatively constant throughout the cluster, with a minor enrichment close to the actin core (Figure 6, A and D). Of importance, similar αMβ2 localization density profiles were found in areas with and without radiating actin filaments (Figure 6A, areas 1 and 2, respectively). To better quantify the distribution of the αMβ2 islets, we subdivided the podosome cluster into three different areas (Supplemental Figure S6) and calculated the average islet density per area. This revealed that the αMβ2 islets within the cluster are equally distributed over areas close to the core or areas with or without actin filaments more distant from the core (Figure 6E). Together these data indicate that the distribution of αMβ2 islets is not guided by the actin network filaments and suggest that the podosome cluster is a well-defined area in the cell marked by a homogeneous enrichment of αMβ2 at the plasma membrane.

Although the localization density of talin appeared higher in areas directly surrounding the podosome core, they displayed only a minor decrease at more distant sites from the core center (Figure 6D). Moreover, we observed that talin, like αMβ2, also did not display a different distribution at regions close to the core or regions with or without actin filaments more distant from the cores (Figure 6, B and E).

By contrast, vinculin is highly concentrated within the direct vicinity of the podosome core, and its levels sharply decrease at increasing distances from the podosome core (Figures 5, B and C, and 6D). However, we observed a remarkable difference in the vinculin distribution in areas with or without radiating actin filaments. In fact, the steep decay in vinculin levels at increasing distances from the core was observed selectively in areas where actin filaments were absent (Figure 6C, area 2). Vinculin levels decrease only gradually at sites containing actin filaments radiating from the core (Figure 6C, area 1). By quantifying the islet density within the podosome cluster, we found that the highest percentage of vinculin islets in the podosome core vicinity (Figure 6E). Of greater importance, the vinculin molecules that are more distant from the podosome core are significantly enriched in areas with actin filaments radiating from the cores compared with actin-free areas (Figures 5, D and E, and 6E). Together these data reveal that vinculin exhibits a heterogeneous localization within the podosome cluster that is guided by the actin network filaments. Together with the notion that vinculin recruitment to talin is tension mediated (del Rio *et al.*, 2009; Kanchanawong *et al.*, 2010; Margadant *et al.*, 2011), our results strongly suggest that within the
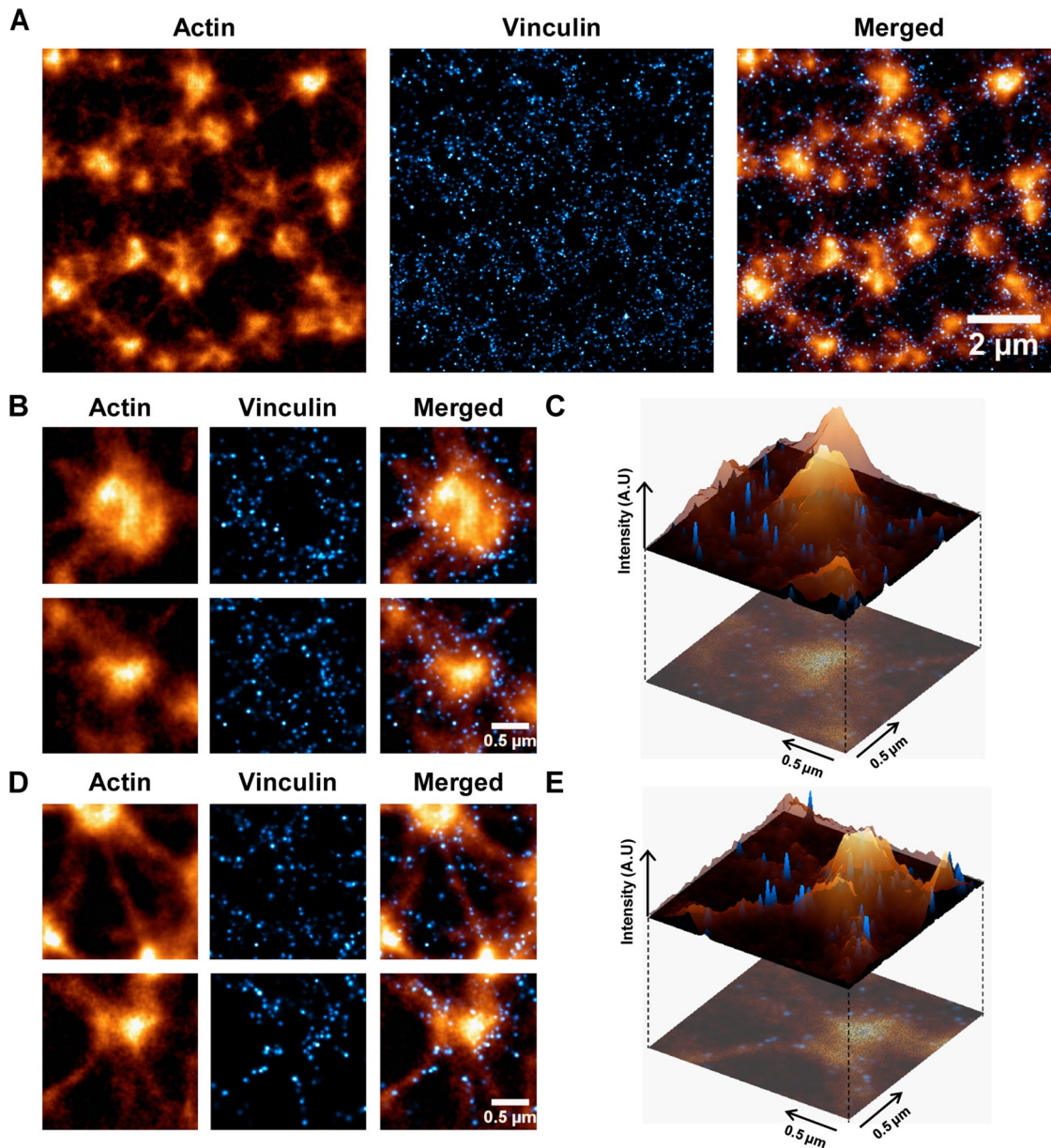
FIGURE 5: Vinculin is found within close proximity of the actin core and aligned with actin filaments. (A) Dual-color dSTORM image of vinculin and F-actin within the podosome cluster of DCs. (B) Magnification of two individual podosomes within the cluster to show the specific localization of vinculin close to the podosome core. (C) Three-dimensional projection of a dual-color dSTORM image that displays a central core of F-actin surrounded by many vinculin islets. The lower image in B is used for this projection. (D) Magnification of two individual podosomes within the cluster to show the colocalization of the vinculin islets with the F-actin network. (E) Three-dimensional projection of a dual-color dSTORM image to show to show the colocalization of vinculin islets with the F-actin network. The lower image in D is used for this projection.

podosome cluster, tension is specifically generated close to the podosome core and along the radiating filaments of the actin network.

DISCUSSION

By applying dual-color dSTORM on adherent human DCs, we demonstrated that podosomes comprise a dense actin core supported by radiating actin filaments that are reinforced by vinculin and anchored onto a layer of homogeneously distributed islets of integrin-bound talin. Of importance, our findings indicate that the "closed" ring structure attributed to podosomes in images obtained by conventional diffraction-limited fluorescence microscopy is in fact lack-

ing. We propose a revised model (Figure 6F) of the podosome architecture incorporating the novel information obtained by superresolution microscopy, in which the adhesive apparatus of podosomes consists of numerous integrin islets. These islets are differentially populated by cytoskeletal adaptor proteins, depending on their association with tensed actin filaments that radiate from and interconnect the protrusive podosome cores. Our model highlights the role of the actin network in organizing the podosome cluster as a mesoscale mechanosensing apparatus and emphasizes the impressive plasticity of actin and actin-binding proteins to ensure the assembly and function of cellular structures that are both adhesive and protrusive.
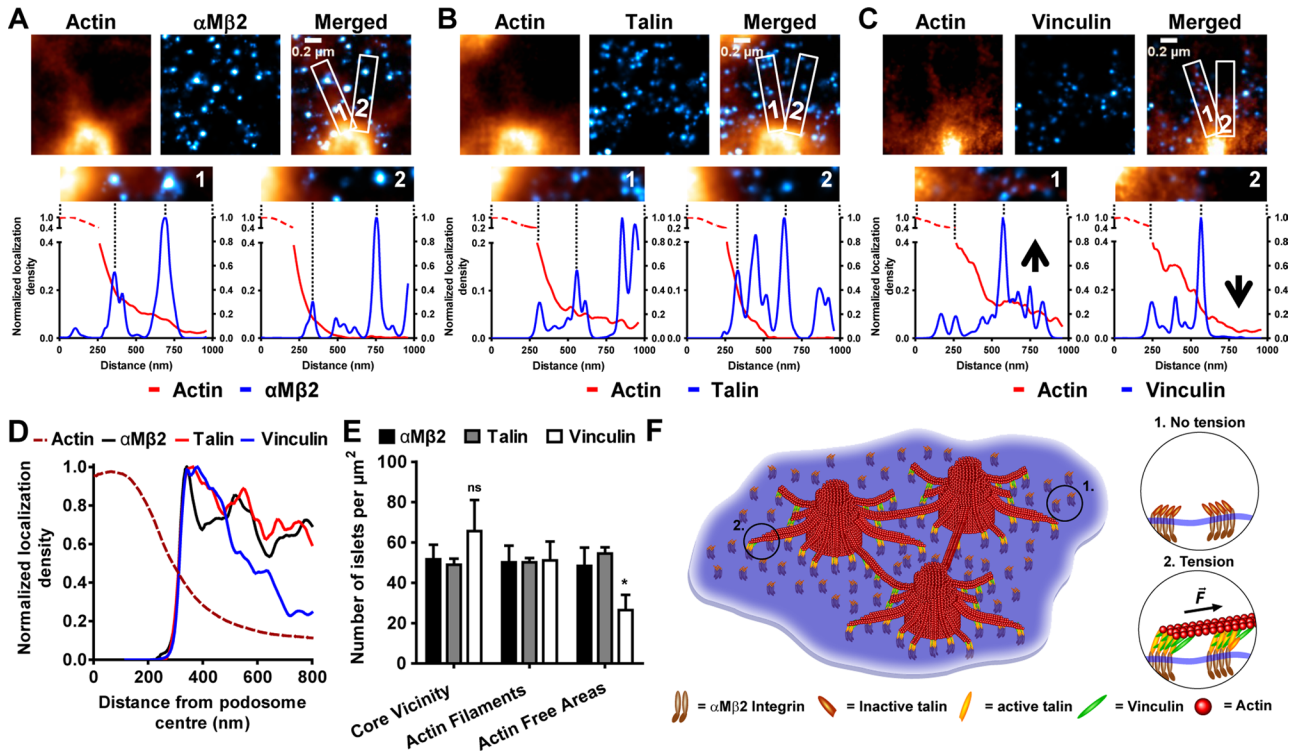
FIGURE 6: Differential distribution of αMβ2, talin, and vinculin within podosome clusters. (A–C) The fluorescence intensity profiles of individual podosomes for actin (red) and (A) αMβ2 (blue), (B) talin (blue), and (C) vinculin (blue) at increasing distance from the podosome center at a site with (1) and without (2) a radiating actin filament. (D) The localization density was measured radially at increasing distances from the podosome core for at least 10 individual podosomes. Shown are the average localization density profiles of αMβ2 (black), talin (red), and vinculin (blue) relative to actin (dotted dark red line). (E) Islet density (islets/square micrometer) within the core vicinity, actin filaments, and actin free areas for αMβ2, talin, and vinculin. (F) Proposed model of a podosome cluster based on dual-color dSTORM superresolution microscopy. Podosome cores are characterized by enormously dense F-actin. The integrin αMβ2 and talin are localized in small islets homogeneously distributed within a podosome cluster but completely excluded from the podosome core areas. This carpet of presumably primed αMβ2 islets is ready to bind to the extracellular matrix, as well as to interacting proteins on the cytosolic side of the membrane. Furthermore, vinculin is selectively localized within close vicinity of the podosome F-actin core and along the interconnecting actin filaments. Because vinculin is known to simultaneously bind to actin and talin, we propose that these vinculin molecules bind to active, stretched talin that is bound to the integrins and is under tension. The tension is generated by podosome core growth within the actin filaments that radiate from the cores and attach to the ventral plasma membrane, potentially functioning as core stabilizers. Actin filaments also interconnect neighboring cores indicating that forces can be transmitted and redistributed over a large range among the podosomes within the cluster. This model combines the protrusive and adhesive properties of individual podosomes, as well as the mechanosensing abilities of the clusters at the mesoscale. Tension-dependent adjustment of the adaptor protein levels within the αMβ2 and talin islets represents a dynamic and highly efficient mechanism for the coordination and feedback regulation of mesenchymal migration within DCs.

Podosomes arrange into higher-ordered structures in many cell types, such as endothelial cells (Tatin *et al.*, 2006) and macrophages (Linder *et al.*, 1999) but most notably in osteoclasts, where they form tightly adhesive belts that constitute the sealing zone and facilitate bone degradation (Jurdic *et al.*, 2006). Here we provide a novel structural framework to further investigate the collective function of podosome clusters. Our work demonstrates that in DCs, the podosome cluster should be regarded as one multifunctional zone consisting of three main substructures: actin-dense cores, integrin islets differentially populated by adaptor proteins, and a well-organized network of filamentous actin radiating from the cores dedicated to protrusion, adhesion, and mechanotransduction, respectively. Protrusion is mediated by the extremely dense podosome cores, most likely driven by continuous actin polymerization at the base of the core and concomitant actomyosin contraction in the F-actin network (Destaing *et al.*, 2003; Gawden-Bone *et al.*, 2010;

van den Dries *et al.*, 2013). Adhesion is mediated by αMβ2 islets, which constitute a homogeneously distributed layer within the podosome cluster and are specifically excluded from the core. Of importance, we observed a similar distribution for αMβ2 and talin within the podosome cluster, suggesting that the integrins are constitutively bound to talin and therefore primed to bind ligands on the extracellular face and recruit adaptor proteins from the cytoplasm (Tadokoro *et al.*, 2003). Similar to the belts in osteoclasts, this adhesive zone appears to be in extremely close contact with the underlying substrate, as indicated by the necessity to permeabilize DCs before integrin staining with antibodies (Supplemental Figure S7B). Finally, mechanotransduction most likely relies on the F-actin network to provide the molecular link between the protrusive actin pillars and the adhesive integrin-talin islets. We here show that this F-actin network is the major determinant for the differential localization of vinculin and talin within the podosome ring. Recently we

demonstrated that the levels of tension-dependent vinculin but not talin oscillate in harmony with the podosome core (van den Dries et al., 2013). The model presented here integrates the novel super-resolution findings and highlights how core growth can generate tension on the radiating actin filaments, driving the specific recruitment of the mechanosensitive protein vinculin to the integrin–talin islets associated with these actin filaments. Besides reinforcing the actin filaments of protruding podosomes, vinculin could be directly involved in organizing and shaping the actin structures at the podosome site in a talin-independent manner, as recently suggested by Wen et al. (2009). By adapting the levels of vinculin at the islets to the tension generated within the radiating actin filaments, the podosomal architecture may facilitate a continuous feedback loop for the cells' local protrusive activity. At the mesoscale level, the network would allow the transmission of mechanical stimuli within and among podosomes throughout a large cluster most likely to coordinate the cells' protrusive and adhesive activity during mesenchymal migration.

Immature DCs reside in peripheral tissues in search of foreign material and exhibit a slow mesenchymal migration, which is characterized by tight interactions with the ECM and active, protease-mediated ECM degradation (Friedl and Weigelin, 2008; Friedl and Wolf, 2010). For mesenchymal migration in three-dimensional collagen matrices, protease activity is concentrated specifically at sites of high physical stress (Wolf et al., 2007). Of interest, we have previously shown that podosomes preferentially form at places with high physical stress (van den Dries et al., 2012), and the transmembrane matrix metalloprotease MT1-MMP has been found at the site of podosomes (Wiesner et al., 2010). These observations, combined with the podosome nanoarchitecture presented here, indicate that podosomes are structures extremely suited to sense and palpate their environment to facilitate mesenchymal migration. On encountering ECM fibers, pressure-induced protease activation at the site of podosomes could induce the focalized pericellular proteolysis of the ECM to further allow the migration of immature DCs through peripheral tissues. The remarkable polarization of many functions associated with migration that converge at the podosome cluster highlights the efficiency with which mesenchymal migration is coordinated in DCs. Future experiments combining high-resolution imaging and three-dimensional imaging setups (Lidke and Lidke, 2012) are needed to further elucidate the role of podosomes in regulating the mesenchymal migration of DCs.

MATERIALS AND METHODS
Preparation of human DCs
DCs were generated from peripheral blood mononuclear cells as described previously (Thurner et al., 1999; de Vries et al., 2002). Monocytes were derived either from buffy coats or from a leukapheresis product. Plastic-adherent monocytes were cultured in RPMI 1640 medium (Life Technologies, Carlsbad, CA) supplemented with fetal bovine serum (FBS; Greiner Bio-One, Frickenhausen, Germany), 1 mM Ultra-glutamine (BioWhittaker; Lonza, Basel, Switzerland), antibiotics (100 U/ml penicillin, 100 µg/ml streptomycin, and 0.25 µg/ml amphotericin B; Life Technologies), IL-4 (500 U/ml), and granulocyte-macrophage colony-stimulating factor (800 U/ml) in a humidified, 5% CO_2–containing atmosphere. For experiments, cells were seeded on uncoated glass coverslips or, where indicated, on glass coverslips with fibronectin, collagen type I, or laminin. For substrate stiffness experiments, cells were seeded onto uncoated 35-mm µ-dishes with an elastically supported surface (Ibidi, Munich, Germany).

Antibodies and reagents
The following antibodies were used: mouse anti-vinculin, mouse anti-talin (Sigma-Aldrich, St. Louis, MO), and mouse anti-αM integrin (clone Bear-1). Alexa Fluor 488–, Alexa Fluor 546–, Alexa Fluor 633–, and Texas red–conjugated phalloidin (Invitrogen, Carlsbad, CA) were used to stain F-actin. For superresolution experiments, antibodies were conjugated with the amine-reactive Alexa Fluor 647 carboxylic acid, succinimidyl ester dye (Invitrogen). Final antibody:dye ratios varied between 1:1 and 1:2.

Labeling
For Figure 2A, vinculin-GFP–transfected cells were treated with 2.5 µg/ml cytochalasin D or left untreated and fixed in 3.7% (wt/vol) formaldehyde in phosphate-buffered saline (PBS) for 10 min. Cells were permeabilized in 0.1% (vol/vol) Triton X-100 in PBS for 5 min and blocked with 2% (wt/vol) BSA in PBS. Subsequently cells were washed with PBS and stained with anti-talin antibody, followed by an Alexa Fluor 647–conjugated monoclonal secondary antibody and Alexa Fluor 546–phalloidin. Finally, the cells were washed five times with PBS and stored in phosphate buffer (PB) at 4°C until imaging. For Figure 2B, VinWT-GFP/vinTL-mCherry double-transfected cells were treated with 2.5 µg/ml cytochalasin D or left untreated and fixed in 2% (wt/vol) formaldehyde in PBS for 15 min. Cells were permeabilized in 0.1% (vol/vol) Triton X-100 in PBS for 5 min and blocked with 2% (wt/vol) BSA in PBS. Subsequently cells were washed with PBS and stained with Alexa Fluor 633–phalloidin. Finally, the cells were washed five times with PBS and stored in PB at 4°C until imaging. Cells were imaged on an FV1000 confocal laser scanning microscope (Olympus, Tokyo, Japan) equipped with argon (488 nm) 559- and 635-nm diode lasers using a PlanApochromatic 63×/1.4 numerical aperture (NA) oil immersion objective.

For superresolution experiments, cells were allowed to adhere for 4 h and fixed in 3.7% (wt/vol) formaldehyde in PBS for 10 min. Cells were permeabilized and stained with an Alexa Fluor 488–conjugated phalloidin and, in the case of double labeling, followed by an Alexa Fluor 647–conjugated monoclonal antibody. Cells were permeabilized in 0.1% (vol/vol) Triton X-100 in PBS for 5 min and blocked with 2% (wt/vol) BSA in PBS. The cells were incubated with Alexa Fluor 647–conjugated monoclonal antibodies for 60 min. For double labeling, cells were subsequently washed three times with PBS and incubated with Alexa Fluor 488–conjugated phalloidin for 15 min. Finally, the cells were washed five times with PBS and stored in PBS at 4°C until imaging. Cells were imaged in the presence of an oxygen-scavenging system including 50 mM β-mercaptoethylamine (MEA; Heilemann et al., 2008) as a reducing agent.

Transfection and live-cell imaging
Transient transfections were carried out with the Neon Transfection System (Invitrogen). Cells were washed with PBS and resuspended in 115 µl of resuspension buffer per 0.5×10^6 cells. Subsequently cells were mixed with 5 µg per 1×10^6 cells per transfection and electroporated. Directly after, cells were transferred to WillCo dishes (WillCo Wells, Amsterdam, Netherlands) with prewarmed medium without antibiotics or serum. After 3 h, medium was replaced by medium supplemented with 10% (vol/vol) fetal calf serum and antibiotics. For live-cell imaging (Supplemental Figure S5), cells were washed with PBS, and imaging was performed in RPMI without phenol red to avoid autofluorescence. Transiently transfected cells were imaged on a Zeiss LSM 510 microscope (Carl Zeiss, Jena, Germany) equipped with a PlanApochromatic 63×/1.4 NA oil immersion objective. The samples were excited with a 488-nm (GFP) argon laser, and images were acquired every 15 s at 37°C.

Superresolution imaging

dSTORM imaging was performed using an inverted microscope (IX71; Olympus America, Center Valley, PA) equipped with an oil-immersion objective 1.45-NA total internal reflection fluorescence objective (U-APO 150×/NA 1.45; Olympus America). A 635-nm diode laser (Radius 635; Coherent, Santa Clara, CA) was used for Alexa 647 excitation, and a 488-nm frequency-doubled diode laser (Spectra-Physics Cyan Scientific; Newport, Irvine, CA) was used for Alexa 488. A quad-band dichroic and emission filter set (LF405/488/561/635-A; Semrock, Rochester, NY) set was used for sample illumination and emission. Emission light was separated onto different quadrants of an Ixon 897 electron-multiplying charge-coupled device (EM CCD) camera (Andor Technologies, South Windsor, CT), using a QuadView imaging system (QV2; Photometrics, Tucson, AZ) with additional emission filters (692/40 and 525/30 nm; Semrock). The EM CCD gain was set to ~200, and frames were 256 × 256 pixels with a pixel size of 0.106 μm. Images were acquired with 100-ms exposure and collected over 10,000–20,000 frames. The sample chamber was mounted in a three-dimensional piezostage (Nano-LPS; Mad City Labs, Madison, WI) with a resolution along the xyz-axes of 0.2 nm. Sample drift was corrected for throughout the imaging procedure using a custom-built stage stabilization routine. Before data acquisition, a reference bead, 0.2 um (535/575; Invitrogen), or a "giant" quantum dot (provided by J. Hollingsworth, Los Alamos, NM; Chen et al., 2008) was found using the MCL nanopositioning stage, and the location of the bead relative to the imaging frame was recorded. After each acquisition of 1000 frames, the stage returned to the recorded bead position, and an updated bead position was determined by fitting the bead position along x, y, and z. The updated bead location along the z-plane was determined by scanning a distance of 250 nm above and below the current plane in 10 sequential steps, fitting a two-dimensional Gaussian distribution to the intensity distribution at each plane, and then fitting a curve of the fit primary sigma factor (PSF) values at each plane to find the z plane for which PSF is minimized. The updated xy position of the bead was found by fitting the center of the two-dimensional Gaussian at the bead's in-focus z position, and the stage was moved to the updated position with mean x, y, and z correction of 6.8, 7.5, and 47.9 nm, respectively, over all acquisitions.

Image reconstruction and data analysis

dSTORM images were analyzed and reconstructed with custom-built MATLAB (MathWorks, Natick, MA) functions as described previously (Smith et al., 2010; Huang et al., 2011). Vinculin, talin, and αMβ2 images were reconstructed from between 930,000 and 2,000,000 fit positions. Actin images were reconstructed from between 9,000,000 and 16,000,000 fit positions. For each image frame, subregions were selected based on local maximum intensity. Each subregion was then fitted to a pixelated Gaussian intensity distribution using a maximum likelihood estimator. Fitted results were rejected based on log-likelihood ratio and fit precision estimated using the Cramér–Rao lower bound values for each parameter fit, as well as intensity and background cut-offs. Multifluorophore analysis was used for fitting of the Alexa 488–phalloidin images, as the duty cycle of Alexa 488 and high density of labeled actin resulted in an active density not successfully fitted with a single-emitter model.

Two-color imaging and image alignment

The choice of Alexa 647 for labeling of ring components and Alexa 488 for labeling of actin was made to ensure the most number of acquired fits. We found that Alexa 488–phalloidin superresolution images revealed similar actin structures to those seen using Alexa 647–phalloidin (data not shown). In contrast, labeling of the ring components vinculin, talin, and Mac1 using Alexa 488 antibodies resulted in drastically undersampled reconstructions when compared with reconstructions seen using Alexa 647 antibodies (data not shown). This is a result of the difference in photophysical properties between Alexa 488 from Alexa 647 under our imaging conditions. A large number of Alexa 488 molecules were lost during the acquisition due to photobleaching or improper fitting. However, the high labeling density of phalloidin, as well as the high concentration of actin within the podosomes, made the underlying resolution of the actin structural distribution robust to suboptimal blinking characteristics. This was not the case for the ring component proteins, as they were not expressed at as high levels and the proteins within the structures were not as densely labeled, making the reconstructed structures more sensitive to any loss of fits. On the basis of these initial findings, we chose throughout the rest of the study to use Alexa 647 to label the ring components and Alexa 488–phalloidin to label the dense actin structures.

Dual-color image acquisitions were performed by imaging Alexa 647 and Alexa 488 sequentially. Alexa 647 was imaged first to prevent photobleaching of the Alexa 488. The same bead was used for both channel stabilizations. The extended imaging time needed for the full two-color acquisition necessitated use of the "giant" qdots for the stabilization because they were found most resistant to photobleaching. To correct for shifts due to chromatic aberrations, channels were aligned using multicolor beads (Tetraspek; Invitrogen). Using our piezostage, we placed a single Tetraspek bead at 225 locations (15 × 15) uniformly distributed across the image window. The emission position in both channels was fitted and recorded. A locally weighted transform between the channels across the image was determined as described in Churchman and Spudich (2008). This transform was then used to convert fits from the Alexa Fluor 488 channel into the Alexa Fluor 647 channel. Registration error was calculated using the transform determined from a uniformly distributed subset of fit positions (8 × 8) to overlay the remaining fit positions (7 × 7). Registration error, calculated as the mean of the Cartesian distance between corresponding points in the two channels, was between 4.8 and 7.6 nm. A channel registration data set was always taken within 3.5 h of any data acquisition. We found this necessary to ensure that the registration transform was relevant and that no alignment drift occurred. Comparison of two registration data sets taken 3 h apart resulted in a cross-transformation error of 13.2 and 43.5 nm when taken 12 h apart.

Quantification

Podosome core analysis for Figure 2, E–H. Ring analysis and core perimeter and area analysis were done with ImageJ 1.45b software (National Institutes of Health, Bethesda, MD). Podosome cores were selected on the basis of intensity. Podosome diameter was calculated using $D = 2(\text{sqrt}[A/\pi])$, where D is the diameter of the podosome core and A is the area. Podosome circularity was calculated using $C = 4\pi A/P^2$, where C is the circularity, A is the area, and P is the perimeter of the podosome core. Nearest-neighbor distance was based on the position of the podosome core center. Size value distributions were fitted with a single Gaussian or with a sum of two Gaussians using Prism 5.03 for Windows software (GraphPad Software, La Jolla, CA).

Localization density in Figure 5D. Podosome cores were randomly selected and segmented in the F-actin image. Subsequently a distance transform was calculated for both the segmentation mask

and its logical complement. From these distance transforms masks were created for pixels at each distance from the boundary of the segmented area, both within the segmented area and in the background. Finally, these masks were used to measure the average localization density in the corresponding image of the ring components vinculin, talin, and αMβ2.

Islet density in Figure 5E. For all three components, five regions of 3×3 μm within a podosome cluster were randomly selected and subdivided into three areas: 1) a ring with a width of 0.28 μm surrounding the core of podosomes (Ring Area), 2) areas without actin cores or actin filaments (Actin Free Areas), and 3) areas containing radiating actin filaments but not within the podosome core or ring area (Radiating Actin Filaments). Next the image was thresholded and islets were identified on the basis of their intensity compared with the background. Subsequently islet density values were calculated for vinculin, talin, and αMβ2 for all three areas, presented as the number of islets/square micrometer.

REFERENCES
Bakolitsa C, Cohen DM, Bankston LA, Bobkov AA, Cadwell GW, Jennings L, Critchley DR, Craig SW, Liddington RC (2004). Structural basis for vinculin activation at sites of cell adhesion. Nature 430, 583–586.

Betzig E, Patterson GH, Sougrat R, Lindwasser OW, Olenych S, Bonifacino JS, Davidson MW, Lippincott-Schwartz J, Hess HF (2006). Imaging intracellular fluorescent proteins at nanometer resolution. Science 313, 1642–1645.

Burns S, Hardy SJ, Buddle J, Yong KL, Jones GE, Thrasher AJ (2004). Maturation of DC is associated with changes in motile characteristics and adherence. Cell Motil Cytoskeleton 57, 118–132.

Chen Y, Vela J, Htoon H, Casson JL, Werder DJ, Bussian DA, Klimov VI, Hollingsworth JA (2008). "Giant" multishell CdSe nanocrystal quantum dots with suppressed blinking. J Am Chem Soc 130, 5026–5027.

Churchman LS, Spudich JA (2008). Colocalization of fluorescent probes: accurate and precision registration with nanometer resolution. In: Single-Molecule Techniques, ed. PR Selvin and T Ha, Cold Spring Harbor, NY: Cold Spring Harbor Laboratory Press, Chapter 4.

Cox S, Rosten E, Monypenny J, Jovanovic-Talisman T, Burnette DT, Lippincott-Schwartz J, Jones GE, Heintzmann R (2012). Bayesian localization microscopy reveals nanoscale podosome dynamics. Nat Methods 9, 195–200.

de Vries IJ, Eggert AA, Scharenborg NM, Vissers JL, Lesterhuis WJ, Boerman OC, Punt CJ, Adema GJ, Figdor CG (2002). Phenotypical and functional characterization of clinical grade dendritic cells. J Immunother 25, 429–438.

del Rio A, Perez-Jimenez R, Liu R, Roca-Cusachs P, Fernandez JM, Sheetz MP (2009). Stretching single talin rod molecules activates vinculin binding. Science 323, 638–641.

Destaing O, Saltel F, Geminard JC, Jurdic P, Bard F (2003). Podosomes display actin turnover and dynamic self-organization in osteoclasts expressing actin-green fluorescent protein. Mol Biol Cell 14, 407–416.

Evans JG, Correia I, Krasavina O, Watson N, Matsudaira P (2003). Macrophage podosomes assemble at the leading lamella by growth and fragmentation. J Cell Biol 161, 697–705.

Friedl P, Weigelin B (2008). Interstitial leukocyte migration and immune function. Nat Immunol 9, 960–969.

Friedl P, Wolf K (2010). Plasticity of cell migration: a multiscale tuning model. J Cell Biol 188, 11–19.

Gaidano G, Bergui L, Schena M, Gaboli M, Cremona O, Marchisio PC, Caligaris-Cappio F (1990). Integrin distribution and cytoskeleton organization in normal and malignant monocytes. Leukemia 4, 682–687.

Gawden-Bone C, Zhou Z, King E, Prescott A, Watts C, Lucocq J (2010). Dendritic cell podosomes are protrusive and invade the extracellular matrix using metalloproteinase MMP-14. J Cell Sci 123, 1427–1437.

Geiger B, Spatz JP, Bershadsky AD (2009). Environmental sensing through focal adhesions. Nat Rev Mol Cell Biol 10, 21–33.

Gingras AR, Ziegler WH, Frank R, Barsukov IL, Roberts GC, Critchley DR, Emsley J (2005). Mapping and consensus sequence identification for multiple vinculin binding sites within the talin rod. J Biol Chem 280, 37217–37224.

Heilemann M, van de Linde S, Schuttpelz M, Kasper R, Seefeldt B, Mukherjee A, Tinnefeld P, Sauer M (2008). Subdiffraction-resolution fluorescence imaging with conventional fluorescent probes. Angew Chem Int Ed Engl 47, 6172–6176.

Hess ST, Girirajan TP, Mason MD (2006). Ultra-high resolution imaging by fluorescence photoactivation localization microscopy. Biophys J 91, 4258–4272.

Huang F, Schwartz SL, Byars JM, Lidke KA (2011). Simultaneous multiple-emitter fitting for single molecule super-resolution imaging. Biomed Opt Express 2, 1377–1393.

Humphries JD, Wang P, Streuli C, Geiger B, Humphries MJ, Ballestrem C (2007). Vinculin controls focal adhesion formation by direct interactions with talin and actin. J Cell Biol 179, 1043–1057.

Jurdic P, Saltel F, Chabadel A, Destaing O (2006). Podosome and sealing zone: specificity of the osteoclast model. Eur J Cell Biol 85, 195–202.

Kanchanawong P, Shtengel G, Pasapera AM, Ramko EB, Davidson MW, Hess HF, Waterman CM (2010). Nanoscale architecture of integrin-based cell adhesions. Nature 468, 580–584.

Kopp P, Lammers R, Aepfelbacher M, Woehlke G, Rudel T, Machuy N, Steffen W, Linder S (2006). The kinesin KIF1C and microtubule plus ends regulate podosome dynamics in macrophages. Mol Biol Cell 17, 2811–2823.

Labernadie A, Thibault C, Vieu C, Maridonneau-Parini I, Charriere GM (2010). Dynamics of podosome stiffness revealed by atomic force microscopy. Proc Natl Acad Sci USA 107, 21016–21021.

Lakkakorpi P, Tuukkanen J, Hentunen T, Jarvelin K, Vaananen K (1989). Organization of osteoclast microfilaments during the attachment to bone surface in vitro. J Bone Miner Res 4, 817–825.

Lidke DS, Lidke KA (2012). Advances in high-resolution imaging—techniques for three-dimensional imaging of cellular structures. J Cell Sci 125, 2571–2580.

Linder S, Nelson D, Weiss M, Aepfelbacher M (1999). Wiskott-Aldrich syndrome protein regulates podosomes in primary human macrophages. Proc Natl Acad Sci USA 96, 9648–9653.

Linder S, Wiesner C, Himmel M (2011). Degrading devices: invadosomes in proteolytic cell invasion. Annu Rev Cell Dev Biol 27, 185–211.

Luxenburg C, Geblinger D, Klein E, Anderson K, Hanein D, Geiger B, Addadi L (2007). The architecture of the adhesive apparatus of cultured osteoclasts: from podosome formation to sealing zone assembly. PLoS One 2, e179.

Marchisio PC, Cirillo D, Naldini L, Primavera MV, Teti A, Zambonin-Zallone A (1984). Cell-substratum interaction of cultured avian osteoclasts is mediated by specific adhesion structures. J Cell Biol 99, 1696–1705.

Margadant F, Chew LL, Hu X, Yu H, Bate N, Zhang X, Sheetz M (2011). Mechanotransduction in vivo by repeated talin stretch-relaxation events depends upon vinculin. PLoS Biol 9, e1001223.

Meddens MBM, Rieger B, Figdor CG, Cambi A, van den Dries K (2013). Automated podosome identification and characterization in fluorescence microscopy images. Microsc Microanal 19, 180–189.

Moser M, Legate KR, Zent R, Fassler R (2009). The tail of integrins, talin, and kindlins. Science 324, 895–899.

Murphy DA, Courtneidge SA (2011). The "ins" and "outs" of podosomes and invadopodia: characteristics, formation and function. Nat Rev Mol Cell Biol 12, 413–426.

Nayal A, Webb DJ, Horwitz AF (2004). Talin: an emerging focal point of adhesion dynamics. Curr Opin Cell Biol 16, 94–98.

Patel B et al. (2006). The activity of the vinculin binding sites in talin is influenced by the stability of the helical bundles that make up the talin rod. J Biol Chem 281, 7458–7467.

Pfaff M, Jurdic P (2001). Podosomes in osteoclast-like cells: structural analysis and cooperative roles of paxillin, proline-rich tyrosine kinase 2 (Pyk2) and integrin alphaVbeta3. J Cell Sci 114, 2775–2786.

Rust MJ, Bates M, Zhuang X (2006). Sub-diffraction-limit imaging by stochastic optical reconstruction microscopy (STORM). Nat Methods 3, 793–795.

Saltel F, Chabadel A, Bonnelye E, Jurdic P (2008). Actin cytoskeletal organisation in osteoclasts: a model to decipher transmigration and matrix degradation. Eur J Cell Biol 87, 459–468.

Schmidt S, Nakchbandi I, Ruppert R, Kawelke N, Hess MW, Pfaller K, Jurdic P, Fassler R, Moser M (2011). Kindlin-3-mediated signaling from multiple integrin classes is required for osteoclast-mediated bone resorption. J Cell Biol 192, 883–897.

Smith CS, Joseph N, Rieger B, Lidke KA (2010). Fast, single-molecule localization that achieves theoretically minimum uncertainty. Nat Methods 7, 373–375.

Tadokoro S, Shattil SJ, Eto K, Tai V, Liddington RC, de Pereda JM, Ginsberg MH, Calderwood DA (2003). Talin binding to integrin beta tails: a final common step in integrin activation. Science 302, 103–106.

Tatin F, Varon C, Genot E, Moreau V (2006). A signalling cascade involving PKC, Src and Cdc42 regulates podosome assembly in cultured endothelial cells in response to phorbol ester. J Cell Sci 119, 769–781.

Thurner B, Roder C, Dieckmann D, Heuer M, Kruse M, Glaser A, Keikavoussi P, Kampgen E, Bender A, Schuler G (1999). Generation of large numbers of fully mature and stable dendritic cells from leukapheresis products for clinical application. J Immunol Methods 223, 1–15.

Trotter JA (1981). The organization of actin in spreading macrophages. The actin-cytoskeleton of peritoneal macrophages is linked to the substratum via transmembrane connections. Exp Cell Res 132, 235–248.

van den Dries K, Meddens MB, de Keijzer S, Shekhar S, Subramaniam V, Figdor CG, Cambi A (2013). Interplay between myosin IIA-mediated contractility and actin network integrity orchestrates podosome composition and oscillations. Nat Commun 4, 1412.

van den Dries K et al. (2012). Geometry sensing by dendritic cells dictates spatial organization and PGE(2)-induced dissolution of podosomes. Cell Mol Life Sci 69, 1889–1901.

van Helden SF, Krooshoop DJ, Broers KC, Raymakers RA, Figdor CG, van Leeuwen FN (2006). A critical role for prostaglandin E2 in podosome dissolution and induction of high-speed migration during dendritic cell maturation. J Immunol 177, 1567–1574.

Wen KK, Rubenstein PA, DeMali KA (2009). Vinculin nucleates actin polymerization and modifies actin filament structure. J Biol Chem 284, 30463–30473.

Wiesner C, Faix J, Himmel M, Bentzien F, Linder S (2010). KIF5B and KIF3A/KIF3B kinesins drive MT1-MMP surface exposure, CD44 shedding, and extracellular matrix degradation in primary macrophages. Blood 116, 1559–1569.

Wolf K, Wu YI, Liu Y, Geiger J, Tam E, Overall C, Stack MS, Friedl P (2007). Multi-step pericellular proteolysis controls the transition from individual to collective cancer cell invasion. Nat Cell Biol 9, 893–904.